Image charge models for accurate construction of the electrostatic self-energy of 3D layered nanostructure devices

John R. Barker[(1)] and Antonio Martinez[(2)]

[(1)] School of Engineering, University of Glasgow, Glasgow G12 8LT, UK.
[(2)] College of Engineering, Swansea University, Swansea SA2 8PP, UK.

E-mail: John.Barker@glasgow.ac.uk

Abstract*:* Efficient analytical image charge models are derived for the full spatial variation of the electrostatic self-energy of electrons in semiconductor nanostructures that arises from dielectric mismatch using semi-classical analysis. The methodology provides a fast compact and physically transparent computation for advanced device modeling. The underlying semi-classical model for the self-energy has been established and validated during recent years and depends on a slight modification of the macroscopic static dielectric constants for individual homogeneous dielectric regions. The model has been validated for point charges as close as one interatomic spacing to a sharp interface. A brief introduction to image charge methodology is followed by a discussion and demonstration of the traditional failure of the methodology to derive the electrostatic potential at arbitrary distances from a source charge. However, the self-energy involves the *local* limit of the difference between the electrostatic Green functions for the full dielectric heterostructure and the homogeneous equivalent. It is shown that high convergence may be achieved for the image charge method for this local limit. A simple re-normalisation technique is introduced to reduce the number of image terms to a minimum. A number of progressively complex 3D models are evaluated analytically and compared with high precision numerical computations. Accuracies of 1% are demonstrated. Introducing a simple technique for modeling the transition of the self-energy between disparate dielectric structures we generate an analytical model that describes the self-energy as a function of position within the source, drain and gated channel of a silicon wrap round gate field effect transistor on a scale of a few nanometers cross-section. At such scales the self-energies become large (typically up to ~100 meV) close to the interfaces as well as along the channel. The screening of a gated structure is shown to reduce the self-energy relative to un-gated nanowires.

Keywords: nanostructures, image charge, electrostatic self-energy, semiconductors, dielectric mismatch, nano-transistors

Subject classification: PACS (2008) 73.63-b

1. Introduction

A *dielectric heterostructure* may be defined as the spatial union of a set of homogeneous regions I (I=1…N) described by permittivities $\varepsilon_I(\mathbf{r})$ that depend on location $\mathbf{r}$ and where the interfaces and surfaces are well-defined. A particle P with point charge Q at $\mathbf{r}_1$ will induce polarisation charges at the interfaces and surfaces that generate a resultant electrostatic field $\phi(\mathbf{r}, \mathbf{r}_1, Q)$ (Figure 1a) that reacts back on the charge to produce an *electrostatic self-energy*

$\Sigma(\mathbf{r_1})$ which varies throughout the system (Figure 1). The self-energy [1] is defined semi-classically by

$$\Sigma(\mathbf{r}) = \lim_{\mathbf{r}_1 \to \mathbf{r}} \quad \tfrac{1}{2} Q\{\phi(\mathbf{r}, \mathbf{r}_1, Q) - \phi_{Coulomb}(\mathbf{r}, \mathbf{r}_1, Q)\} \tag{1}$$

where

$$\phi_{Coulomb}(\mathbf{r}, \mathbf{r}_1, Q) = \frac{Q}{4\pi\varepsilon_1 \mid \mathbf{r} - \mathbf{r}_1 \mid} \tag{2}$$

is the Coulomb field of the point charge P in an infinite homogeneous dielectric (bulk) with permittivity $\varepsilon_1=\varepsilon(\mathbf{r}_1)$ (Figure 1b). For dielectric heterostructures with regions with nanometer dimensions the electrostatic self-energies of carriers and charged impurities may be high (meV to a few eV, [1]). Here we focus on semiconductor nanostructures including wrap-round-gate field effect nanowire transistors [2-6] but the following is applicable also to biological systems such as ion channels and to molecular heterostructures including carbon nanostructures. For semiconductor nanostructures the electrostatic self-energy (when considered at all) is generally pre-computed numerically along with a tight-binding evaluation of nanostructure energy band structure [7]. As pointed out in [2, 8-9] the interaction between a charge carrier and its own image charge distribution is a long-range correlation effect, which is not included in the conventional *quantum* many-body theories of out of equilibrium open systems. It should be described within a many-body framework such as the GW method of Hedin and Lundqvist [10,11]. However, the semi-classical electrostatic self-energy with minor modifications (section 2) has been shown to be important for semiconductor nanostructures [8, 7] where it is evaluated by intensive numerical methods.

The underlying semi-classical model for the self-energy has been established and validated during recent years [1-2, 7-9, 20-23] and depends on a slight modification of the macroscopic static dielectric constants for individual homogeneous dielectric regions. The modification involves in the role of dynamic screening. For strong dielectric mismatch e.g for the silicon-silicon dioxide interface, a modified dielectric constant must be used that differs from the bulk obtained by subtracting the ionic contribution (which responds very slowly to electrons moving in a nanowire [1-2, 25]]). A similar argument applies to the choice of modified dielectric constant in III-V semiconductors but not to silicon or SiGe. The underlying model has been validated for point charges as close as one inter-atomic spacing to a sharp interface [19] and to a few silicon planes [23]. In the present work the model is used to compute self-energies for point charges in an environment determined electrostatically by a modified static dielectric function. The intended target is the incorporation of the self-energy into full quantum transport studies [3-6] of nanostructured devices using the self-consistent Keldysh non-equilibrium Green function methodology. The latter methodology quantizes the system in the position representation so that the resulting electronic properties are parameterized by states that depend on the electrostatic self energy which acts like an addition to the confinement potential but as we show later (section 5) may vary spatially along a homogeneous device channel with values between ~ 0 to 100 meV close in magnitude to standard confinement energies. In this fashion the relatively simple classical self-energy enters directly into the complex scenario of electronic states and their dependence on the underlying crystalline geometry.

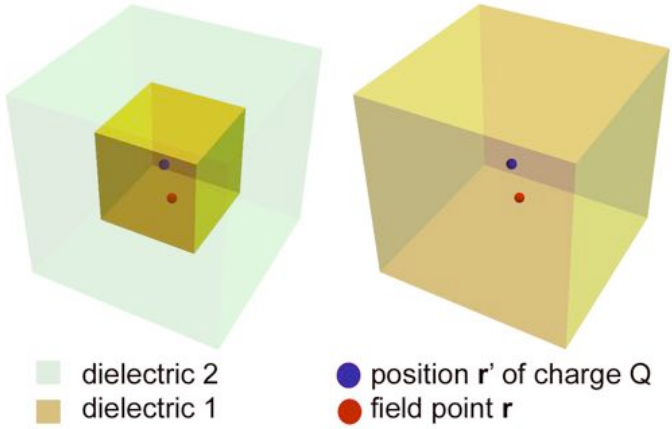

(a) (b)

Figure 1: (a) Charge Q at $\mathbf{r}'$ in a volume of dielectric 1 enclosed by dielectric 2 gives rise to an electrostatic potential $\varphi_{12}(\mathbf{r}) = (1/4\pi\,\varepsilon)/|\mathbf{r}\text{-}\mathbf{r}'| + \varphi_{induced}(\mathbf{r})$ at the field point $\mathbf{r}$. (b) Charge Q at $\mathbf{r}'$ in bulk homogeneous dielectric 1 and a field point $\mathbf{r}$ where the potential is $\varphi_1(\mathbf{r}) = (1/4\pi\varepsilon)/|\mathbf{r}\text{-}\mathbf{r}'| \neq \varphi_{12}(\mathbf{r})$. The potential $\varphi_{induced}(\mathbf{r})$ results from the charge induced at the interfaces by source charge Q.

In the present paper we demonstrate that there are excellent prospects for deploying accurate *compact analytical models* for the electrostatic self-energy based on image charge methods. The aim is to promote better understanding of the key physical processes and effective device design without complex numerically intensive computing. The approach utilises image charge methods without recourse to slowly convergent series or multiple integrations and without special methodologies [12] developed for solvation problems such as particle-mesh Ewald methods, fast multi-pole methods, and others for which compact analytical models are not available. In section 3 we consider two parallel grounded conducting slabs separated by a distance d and determine the electrostatic potential along a central line at a distance D=10d from a point charge. It is found that 1% accuracy requires the summation of 10^6 images as first conjectured in [13]. This problem is generally present for computing the electrostatic potential in dielectric heterostructures, but not for the evaluation of the self-energy. It is shown in section 3 that the *localised* nature of the self-energy requires many fewer image charge summations and indeed using a simple renormalisation scheme may reduce the number to less than 10 for accuracies better than 1%.

The determination of the image potential $\phi_{\text{Image}}(\mathbf{r}, \mathbf{r}_1, Q)$ from a summation over image charges is well-known [13] to have convergence problems for large separations of the field point and the source point $|\mathbf{r} - \mathbf{r}_1| >> 0$, because the resultant series are *asymptotic*. However, as we shall demonstrate, the construction of the self-energy involves the *local* limit $|\mathbf{r} - \mathbf{r}_1| \to 0$ leading to rapid convergence provided a position-independent contribution to the self-energy is correctly identified.

The plan of the paper involves a simple introduction to the electrostatic self-energy including archetypal models for the image charge representation (in section 2). Section 3 describes infinite planar layered dielectric heterostructures. Section 4 describes infinite nested square cross-section dielectric heterostructures. Section 5 introduces a methodology to extend the image methodology to adjoining nested square boxed structures with *finite* dimensions including wrap-round-gate silicon nanowire field effect devices. Section 6 considers briefly the extension to cylindrical layered dielectric heterostructures.

2. The electrostatic self-energy

2.1 General

The self-energy $\Sigma(\mathbf{r})$ is defined in equation (2). The factor ½ is slightly counter-intuitive since for interactions between *different* particles we expect a factor of 1. Here it is derived in more detail. The starting point is Poisson's equation that describes the electrostatic potential set by a charge density $\rho(\mathbf{r})$ for a scalar permittivity function $\varepsilon(\mathbf{r})$ (that describes the dielectric heterostructure) plus appropriate boundary conditions:

$$\nabla.\ \varepsilon(\mathbf{r})\nabla\phi(\mathbf{r}) = -\rho(\mathbf{r}) \qquad (3)$$

The Green function for the Poisson equation satisfies (for the same boundary conditions):

$$\nabla.\ \varepsilon(\mathbf{r})\nabla g(\mathbf{r},\mathbf{r}_1) = -\delta(\mathbf{r}-\mathbf{r}_1) \qquad (4)$$

A particle *P* with point charge *Q* at $\mathbf{r}_1$ will induce polarisation charges at the interfaces and surfaces that generate a resultant electrostatic field $\phi(\mathbf{r}, \mathbf{r}_1, Q)$ given by:

$$\phi(\mathbf{r},\mathbf{r}_1,Q) = Qg(\mathbf{r},\mathbf{r}_1;\varepsilon(\mathbf{r})) \qquad (5)$$

on the other hand, if the particle *P* was in a homogeneous infinite medium with uniform permittivity $\varepsilon_1 = \varepsilon(\mathbf{r}_1)$ we recover the Coulomb potential:

$$\phi_{Coulomb}(\mathbf{r},\mathbf{r}_1,Q) = Qg_0(\mathbf{r},\mathbf{r}_1;\varepsilon_1 \equiv \varepsilon(\mathbf{r}_1)) = \frac{Q}{4\pi\varepsilon_1 |\mathbf{r}-\mathbf{r}_1|} \qquad (6)$$

The *self-field* $\phi_{Self}(\mathbf{r}, Q)$ within a bounded region of homogeneous permittivity ε_1 is defined as the *local limit* of the difference between $\phi(\mathbf{r}, \mathbf{r}_1, Q)$ and the source Coulomb potential:

$$\phi_{Self}(\mathbf{r},Q) = \lim_{\mathbf{r}_1\to\mathbf{r}} \{\phi(\mathbf{r},\mathbf{r}_1,Q) - \phi_{Coulomb}(\mathbf{r},\mathbf{r}_1,Q)\} = \lim_{\mathbf{r}_1\to\mathbf{r}} Q\{g(\mathbf{r},\mathbf{r}_1) - g_0(\mathbf{r},\mathbf{r}_1;\varepsilon_1)\} \quad (7)$$

The self-field is the additional electrostatic potential of the particle P due to the presence of a surfaces and interfaces of the polarisable heterostructure. To construct the self-energy Σ let us consider the self-field $\phi_{Self}(\mathbf{r}, q)$ due to a smaller charge $|q|<|Q|$; then an infinitesimal increment in the charge δq will lead to *P* experiencing an infinitesimal increase in the interaction self-energy $\delta\Sigma = \delta q\ \phi_{Self}(\mathbf{r}, q)$ (in the limit: $d\Sigma/dq = \phi_{Self}(\mathbf{r}, q)$). Here we used the property that $\phi_{Self}(\mathbf{r}, q)$ is directly proportional to *q* (equation (7)*)*. The full self-energy is therefore the result of building up the charge to its final value Q:

$$\Sigma(\mathbf{r}) = \int_0^Q \phi_{Self}(\mathbf{r},q)\,dq = \tfrac{1}{2}Q\phi_{Self}(\mathbf{r},Q) \qquad (8)$$

in agreement with equation (1) of section 1. Or in terms of the Green function for Poisson's equation:

$$\Sigma(\mathbf{r}) = \lim_{\mathbf{r}_1\to\mathbf{r}} \tfrac{1}{2}Q^2\{g(\mathbf{r},\mathbf{r}_1) - g_0(\mathbf{r},\mathbf{r}_1;\varepsilon_1)\} \qquad (9)$$

2.2 The archetypical model: two layered dielectric slabs

The simplest example of the construction of the electrostatic self-energy is sketched in Figure 2. A point charge Q is located in a uniform dielectric I_1 ($\varepsilon=\varepsilon_1$) at $\mathbf{r}_1= (x_1,y_1, z_1)$ at a distance $d=b-y$ from the planar interface with a uniform dielectric I_2 (occupying, $y\geq b$ for all x, y; $\varepsilon=\varepsilon_2$). The problem is trivially solved by the method of images, but we shall illustrate the field-theoretic approach that may be used very generally as a method for the rigorous extraction of image charges. A useful preliminary is to note that in this geometry the simple Coulomb field of the point charge in bulk dielectric with $\varepsilon=\varepsilon_1$ (no interfaces) is:

$$\phi_C(\mathbf{r},\mathbf{r}') = \frac{Q}{4\pi\varepsilon_1 |\mathbf{r}\text{-}\mathbf{r}'|} = \frac{Q}{4\pi\varepsilon_1\sqrt{(x-x_1)^2+(y-y_1)^2+(z-z_1)^2}}$$
$$= \frac{Q}{4\pi\varepsilon_1\sqrt{(y-y_1)^2+\rho^2}} \quad = \frac{Q}{4\pi\varepsilon_1}\int_0^\infty J_0(k\rho)e^{-k|y-y_1|}dk \tag{10}$$

In region I_1 the general solution comprises a Coulomb term plus a solution to the homogeneous Poisson equation (Laplace's equation):

$$\varphi_1 = \frac{Q}{4\pi\varepsilon_1}\int_0^\infty J_0(k\rho)\{e^{-k|y-y_1|} + Ae^{ky}\}dk \tag{11}$$

$$\varphi_2 = \frac{Q}{4\pi\varepsilon_1}\int_0^\infty J_0(k\rho)Ce^{-ky} \tag{12}$$

These forms satisfy the correct boundary conditions at infinity. The coefficients A and C are determined by matching ϕ_1, ϕ_2 *and* $\varepsilon_1\partial\phi_1/\partial y$, $\varepsilon_2\partial\phi_2/\partial y$ at $y=b$. This leads to:

$$A = \frac{\varepsilon_1-\varepsilon_2}{\varepsilon_1+\varepsilon_2}\exp[-k(2b-y-y_1)] \tag{13}$$

From (13) and using the identity (10) we find:

$$\phi_{Self}(y) = \lim_{\rho\to 0}\frac{Q}{4\pi\varepsilon_1}\int_0^\infty J_0(k\rho)e^{-2k|b-y|}dk = \frac{Q}{4\pi\varepsilon_1}\frac{\lambda_{12}}{2(b-y)} \tag{14}$$

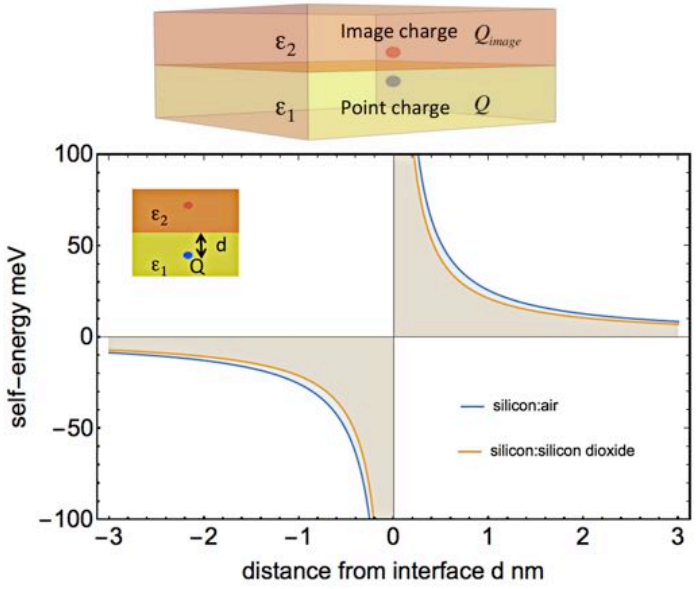

Figure 2: Image charge model: two infinite parallel dielectric slabs: single interface
Showing source and image charges and variation of electrostatic energy as a function of the distance d of the charge Q from the interface for dielectric I_1= silicon (ε_1=11.87 ε_0) and dielectric I_2 = air (ε_2=ε_0) or silicon dioxide (ε_2=2.1 ε_0).

Here, we encounter the factor

$$\lambda_{12} = \frac{\varepsilon_1 - \varepsilon_2}{\varepsilon_1 + \varepsilon_2} = -\lambda_{21} \qquad (15)$$

The self-energy then follows as

$$\Sigma(\mathbf{r}) = \frac{\lambda_{12} Q^2}{16\pi\varepsilon_1} \frac{1}{b-y} = \frac{\lambda_{12} Q^2}{16\pi\varepsilon_1} \frac{1}{d} \qquad (16)$$

Here, d=b-y as the distance of the source charge from the interface or better, 2d is the separation of the source charge from an *image charge* Q_{Image}=$\lambda_{12}Q$, at y_{Image}=y+2d. Figure 2 shows the configuration for this example and the self-energy in regions I_1 and similarly in I_2 for silicon and air and silicon and silicon dioxide. An important detail that differs from a purely classical treatment is that for the oxide we adopt a value for ε =2.1 ε_0 that corresponds to just the electronic contribution as described in [8] for the semi-classical self-energy. In the case that dielectric I_2 is replaced by a conducting slab, we may use the limit $\varepsilon_2 \to \infty$; then the self-energy only exists in the lower half plane (d>0) and the image charge becomes –Q in the above formulae. Physically, it apparent that the electrostatic energy for Q less than a few nm from a region of strong dielectric mismatch is of the order of quantum confinement energies (less than to the order of 1 eV).

More general models involving multiple slabs both above and below I_1 may be handled similarly except that an additional term Bexp[-ky] is required in equation (11) and the other regions will again involve exponentials of the form exp[±ky] with different coefficients

determined by the boundary conditions at the different interfaces. The coefficients A and B are thus determined to be functions of the interface parameters, the permittivities and k. By expressing the k-dependence of these coefficients solely in terms of exponentials in k, the self-potential and self-energy in I_1 is obtained in the form of a sum over images

$$\phi_{Self}(y) = \lim_{\rho\to 0} \frac{Q}{4\pi\varepsilon_1} \int_0^\infty J_0(k\rho) \sum_{\text{Image}} \lambda_{\text{Image}} e^{-k|y_{\text{Image}}-y|} dk = \sum_{\text{Image}} \frac{1}{4\pi\varepsilon_1} \frac{\lambda_{\text{Image}} Q}{|y - y_{\text{Image}}|} \quad (17)$$

$$\Sigma(\mathbf{r}) = \sum_{\text{Image}} \frac{1}{8\pi\varepsilon_1} \frac{\lambda_{\text{Image}} Q^2}{|y - y_{\text{Image}}|} \quad (18)$$

which is a sum over image locations y_{Image} and effective image charges λ_{Image}Q (*Image*=1,2,…).

3. Image charge models: three parallel dielectric slabs

3.1 Dielectric sandwiched between a dielectric slab and a conducting slab

The first non-trivial model for the image charge computation of the electrostatic self-energy energy is provided by a point charge Q at (x_1,y_1,z_1) in a dielectric slab (I_1) in the region $y_1 \le b$ ($b>0$) where $b<y \le a=b+t$ locates a second dielectric slab (I_2) and the region y > a is occupied by a *grounded conductor* (I_3). The configuration is sketched in Figure 3. The electrostatic field within the region $y<b$ comprises the source Coulomb potential due to the charge Q and the Coulomb fields resulting from an *infinite* number of image charges Q_{image} located at y_{image}:

$$\begin{aligned} y_{image} &= 2b - y, \;\; Q_{image} = \lambda_{12} \\ y_{image} &= 2b - y + 2t, \;\; Q_{image} = (1-\lambda_{12}^2)\lambda_{23} \\ y_{image} &= 2b - y + 2Nt, \;\; Q_{image} = -\frac{(1-\lambda_{12}^2)}{\lambda_{12}} (\lambda_{21}\lambda_{23})^N \quad (N = 2,3,...\infty) \end{aligned} \quad (19)$$

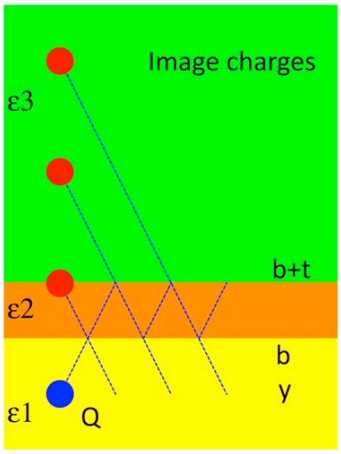

Figure 3: Image charge model: three infinite parallel dielectric slabs: two interfaces Showing source Q and construction of image charges.

Here, a direct construction by ray tracing to locate the image charges utilises: a reflection coefficient λ_{12} from travel from source Q towards the first interface ($y \le b$); a transmission coefficient $(1-\lambda_{12})$ across the first interface $y=b$; a reflection coefficient (λ_{23}) at the second interface $y=b+t$; a reflection coefficient λ_{21} and transmission coefficient $(1-\lambda_{21})=(1+\lambda_{12})$ at the lower interface y=b. Multiple ray paths lead to multiple images as sketched in Figure 3 . The resulting electrostatic self-energy for region $y \le b$ is easily obtained and may be verified by a straightforward field theoretic methods (as in section 2):

$$\Sigma(\mathbf{r}) = \frac{Q^2}{16\pi\varepsilon_1}\{\frac{\lambda_{12}}{b-y} - (1-\lambda_{12}^2)\sum_{N=1}^{\infty}\frac{(\lambda_{21}\lambda_{23})^N}{\lambda_{12}(b-y+Nt)}\} \tag{20}$$

This summation may be evaluated with the aid of the Lerch function [14]

$$\Phi_L(\beta,1,\alpha) = \sum_{N=0}^{\infty}\frac{\beta^N}{\alpha+N} = \int_0^{\infty}\frac{e^{-\alpha u}}{1-\beta e^{-u}}\mathrm{d}u \tag{21}$$

$$\Sigma(\mathbf{r}) = \frac{Q^2}{16\pi\varepsilon_1}\{\frac{\lambda_{12}}{d} - \frac{(1-\lambda_{12}^2)}{\lambda_{12}}\{\Phi_L(\lambda_{21}\lambda_{23},1,d/t)-t/d\}\} \tag{22}$$

where $d=b-y$.

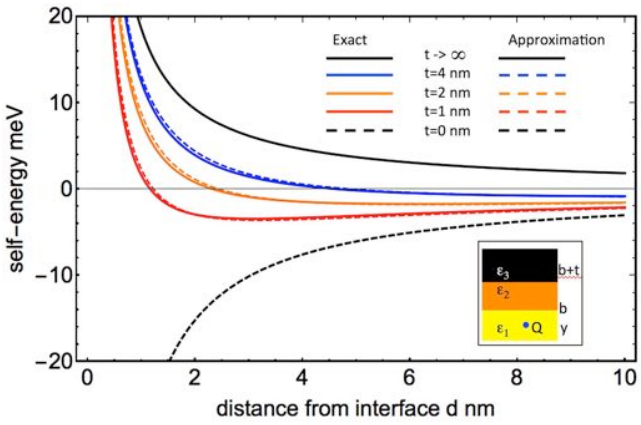

Figure 4. Self-energy of an electron (charge Q) as a function of the perpendicular distance $d=b-y$ from the I_1- I_2 interface at $y=b$ in the silicon component of a dielectric heterostructure comprising parallel planar slabs (I_1 = silicon, I_2 = oxide, I_3 = grounded conducting slab (part of the cross-section shown as an inset). Exact theory (full curves). Approximate theory from equation (23)(dashed curve) for oxide thickness t=1 nm, 2 nm, 4 nm, infinity; the case t=0 is exact in both the approximate and exact theory (black dashed curve). Oxide permittivity =0.287 ε_0 ; semiconductor permittivity 11.87 ε_0.

In the case that λ_{23}= -1 (conducting slab) illustrated in Figure 4 we may use an appropriate series expansion of the Lerch function [14] to find a good approximation valid for $t<d$ (we note the cancellation of terms from the second image) :

$$\Sigma(\mathbf{r}) \sim \frac{Q^2}{16\pi\varepsilon_1}\{\frac{\lambda_{12}}{d} - \frac{1+\lambda_{12}}{d+2t}\} \tag{23}$$

Approximation (23) is exact for ($t \to \infty$) and ($t \to 0$). Figure 4 exhibits the accuracy of the approximation for a point electronic charge of $|e|$ in silicon close to a gated oxide region ($\varepsilon_2=2.87\varepsilon_0$) of thickness t=4 nm, 2 nm, 1 nm (dashed blue, red, orange curves) compared with the exact self-energy (solid blue, red, orange curves). A very thick oxide ($t \to \infty$) is shown by the exact black curve whereas the exact dashed black curve corresponds to t=0. The distance of the charge from the b=1 interface is varied between 0.25 nm to 10 nm. The accuracy of the approximation (23) involving just two effective image charges is better than 1%. The exact solution is given by (20) or (22) or by an integral form derived by field theory in the Appendix where we also displayed the error computation. This is an interesting case that shows the action of a gated thin oxide in reducing the self-energy of an electron in silicon relative to that of a thick oxide.

3.2 Dielectric sandwiched between two conducting slabs

The next order of complexity is provided for the self-energy within the central of three parallel dielectric slabs. The simplest version involves a dielectric sandwiched between two parallel grounded conducting slabs with interfaces at $y=\pm b$. Here the image map is illustrated in Figure 5. It comprises a periodic array of copies of the original charge Q and the nearest image charge ($-Q$).

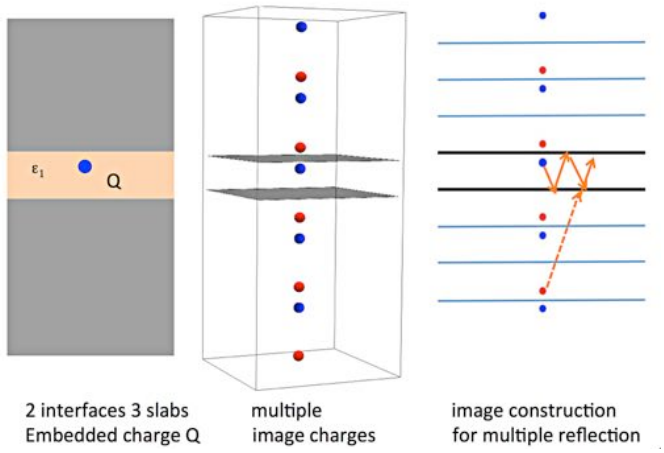

(a) (b) (c)

Figure 5: Image charge model: (a) charge Q embedded in a dielectric between two conducting slabs; (b) shows location of multiple image charges and the two interfaces. (c) Shows the construction of one of the images by ray paths. Blue dots represent charge $+Q$, Red dots correspond to $-Q$.

In the central dielectric the electrostatic potential at a field point $\mathbf{r}=(x,y,z)$ comprises the sum of the Coulomb fields from the source charge and an infinite number of image charges of value $\pm Q$:

$$\phi(y,\rho)=\frac{1}{4\pi\varepsilon_1}\sum_{N=-\infty}^{\infty}\{\frac{Q}{\sqrt{(y-y_1+4bN)^2+\rho^2}}+\frac{-Q}{\sqrt{(y+y_1+2b(2N+1))^2+\rho^2}}\} \quad (24)$$

The source potential is given by the N=0 in the first series of equation (24). The image locations along the y-axis and charge assignments are:

$$Q_{\text{Image}} = Q; \quad y_N = y_1 \pm 4bN \qquad (N = 1, \infty)$$
$$Q_{\text{Image}} = -Q; \quad y_N = -y_1 - 2b(2N+1) \qquad (N = -\infty, \infty) \tag{25}$$

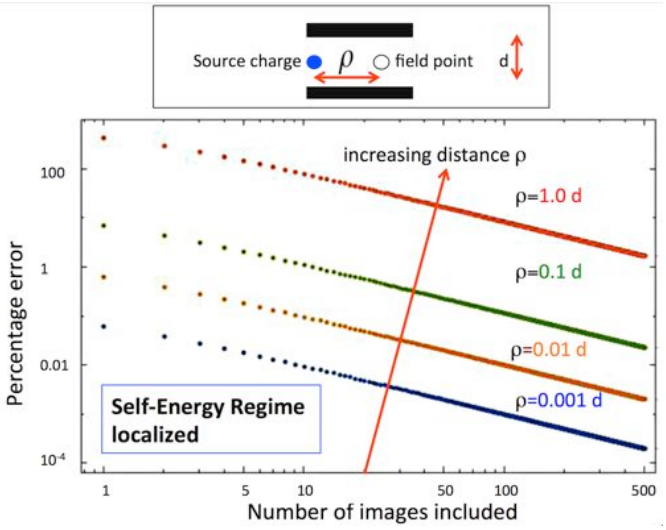

Figure 6: Error in the electrostatic potential as a function of number of image charges for various separations of the field point and the source charge. The percentage error is defined as $100(\phi(y,\rho)_N - \phi(y,\rho)_{exact})/\ \phi(y,\rho)_{exact}$.

Figure 6 displays the percentage error in the computed electrostatic potential as a function of the number of included images at various distances down the channel from the source charge. For a separation of source charge and field point ρ=10d (where here $d=2b$ is the distance between the two conducting slabs) and an accuracy in the potential of the order of 1% requires ~ 10^8 image charges, a result first observed in reference [6]. This slow convergence disappears for shorter distances between the source charge and the field point, precisely the *localised* regime where the self-energy is defined.

The self-energy is obtained as:

$$\Sigma(y) = \frac{Q^2}{8\pi\varepsilon_1}\sum_{N=1}^{\infty}\{\frac{-b(2N-1)}{(2N-1)^2b^2 - y^2} + \frac{1}{2Nb}\} \tag{26}$$

3.3 Dielectric sandwiched between two dielectric slabs

Replacing the two conducting slabs of section 3.2 with dielectric slabs having permittivity ε_2, yields the self-energy as

$$\Sigma(y) = \frac{Q^2}{8\pi\varepsilon_1}\sum_{N=1}^{\infty}\{\frac{b\lambda_{12}^{(2N+1)}(2N-1)}{(2N-1)^2b^2 - y^2} + \frac{\lambda_{12}^{2N}}{2Nb}\} \tag{27}$$

The series has been slightly re-arranged to give symmetric behaviour about y=0 and to give a convergent result at y=0. The nearest images contribute to the leading terms to the self energy except for the central location y=0 where very large numbers contribute.

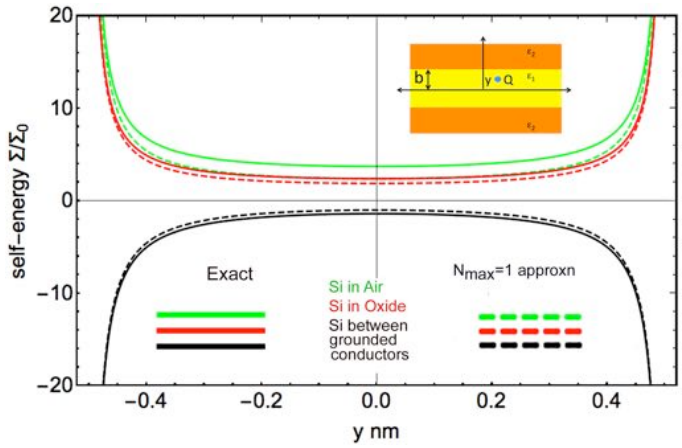

Figure 7: Comparison of the computed electrostatic self-energy for: a single electronic charge in a silicon slab sandwiched between: two grounded conducting slabs (black); two oxide slabs (red); and two regions filled with air. The approximations for N_{max}=1 (eqn 28) are shown with dashed lines. Exact results are shown as full lines. The half-width b = 0.5 nm.

Close to each interfaces the self-energies behave like the single interface result (16). Truncating the summation (27) at N=$N_{\max}$=1 gives :

$$\Sigma(y) = \frac{Q^2}{8\pi\varepsilon_1}\{\frac{\lambda_{12} b}{b^2 - y^2} + \frac{\lambda_{12}^2}{2b}\} = \frac{Q^2}{16\pi\varepsilon_1}\{\frac{\lambda_{12}}{b-y} + \frac{\lambda_{12}^2}{b} + \frac{\lambda_{12}}{b+y}\} \quad (28)$$

Figure 7 compares the $N_{\max}$=1 approximation with the exact self-energy. The results show that equation (28) is a fair approximation near the interfaces but is less accurate at the symmetry point. The N_{max} =2 case has errors of order 20% that reduce to 0.1% with the order of 500 iterations (N_{max}~ 500). However, the main part of the error comes from a constant shift arising from the large number of images that contribute to the centre value Σ(y=0).

3.4 A simple re-normalisation procedure

Since the major source of error in the self-energy comes from a slowly varying term peaking at the symmetry point y=0 it is pertinent to set up a simple re-normalisation scheme where it is supposed that an accurate value for the centre value Σ(y=0) is known. A re-normalised calculation of the self-energy truncated at N=N_{max} may then be written:

$$\Sigma_R(y, N_{\max}) = \Sigma(y, N_{\max}) + \Sigma(y=0) - \Sigma(y=0, N_{\max}) \quad (29)$$

where Σ(y, $N_{\max}$) is given by expression (27) truncated at N= $N_{\max}$. The re-normalised self-energy is thus fixed at the exact value. Figure 8 shows the error in the truncated self energy and the re-normalised self-energy as a function of $N_{\max}$ in the grounded slab case λ_{12}=-1.

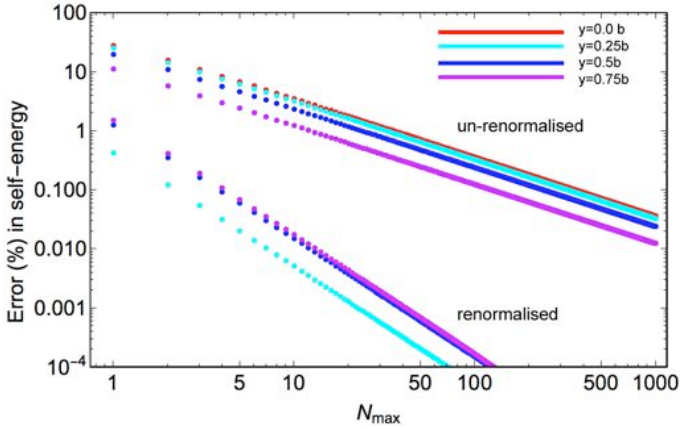

Figure 8: Percentage error in the electrostatic self-energy for a single electronic charge in a silicon slab sandwiched between two grounded conducting slabs as a function of N_{max} and distance y for un-renormalised and normalised expression (half-width b=0.5).

In general the re-normalisation scheme yield two orders of magnitude improvement. The N_{max}=2 approximation is better than 1%. These findings are corroborated in Figure 9 that shows the detailed error in the truncated self-energy (dashed lines) re-normalised truncated self-energy approximation (full lines). The error for the re-normalised self-energy increases towards the interfaces, peaking at about 75% of the half-width b.

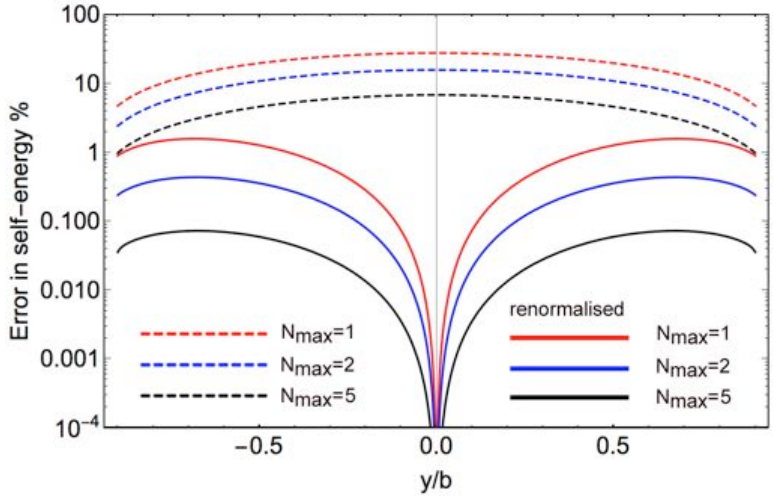

Figure 9: Percentage error in the electrostatic self-energy for a single electronic charge in a silicon slab sandwiched between two grounded conducting slabs as a function of distance y for N_{max}=1,2,5 using un-renormalised and renormalized expressions (for half-width b=0.5 nm).

4. Image charge models: nested dielectric blocks with planar interfaces

4.1 A simple case: a wrap-round square cross sectional dielectric box

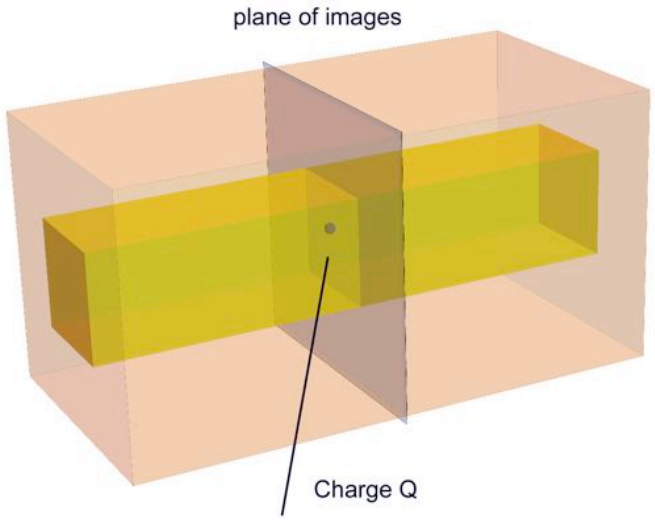

Figure 10. An infinite dielectric box I_1 surrounded by a single dielectric I_2. A charge Q in I_1 is associated with image charges in the plane perpendicular to the main axis that passes through Q.

New features arise in this case: (i) given a charge Q at (x,y,z) belonging to the core dielectric I_1 the image plane (the x-y plane) passes perpendicular to the central z-symmetry axis as shown in Figure 10; (ii) the appearance of corner regions leads to new image charges (shown in Figure 11 for the nearest images to a charge Q near to a corner).

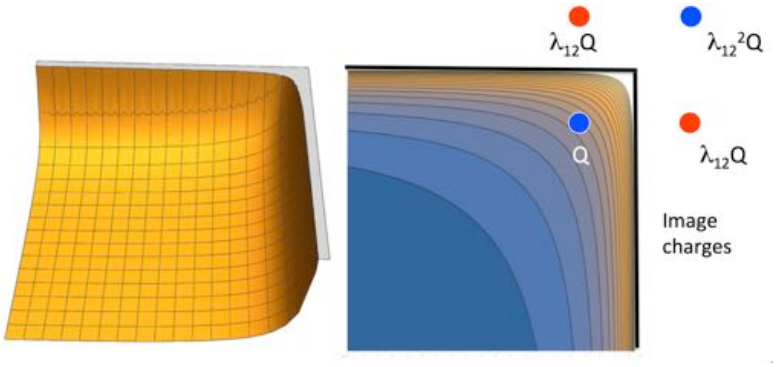

Figure 11: Corners and image charges. On the left is exhibited the self-energy in landscape mode over the x-y plane; on the right a contour plot of the self-energy near a corner in the image plane is combined with diagrams showing the location of the source charge Q and the nearest image charges and their locations.

The spatial locations of the nearest images may be exhibited as an image location map (Figure 12 shows 99 nearest image charges for the central solution domain containing a single source charge Q). The corresponding image charge assignment is shown in Figure 13.

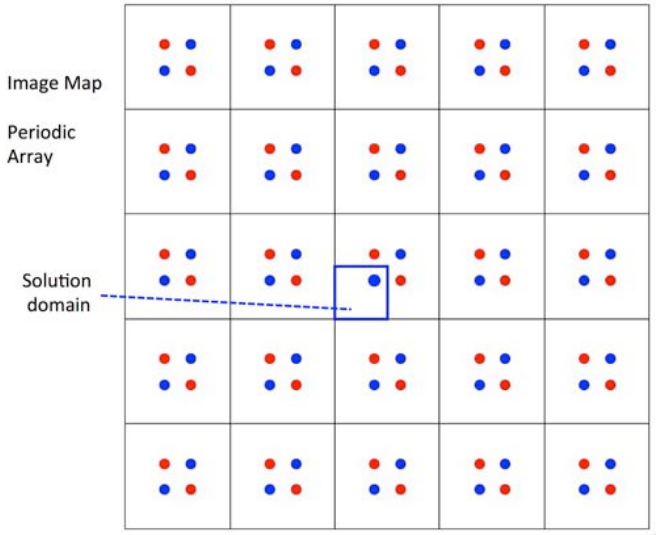

Figure 12. Image map for 2 nested boxes. The location of charge Q within region 1 (box 1) bounded by an infinite region 2(box 2) is the solution domain where it is required to evaluate the self-energy. The charge Q creates image charges within the periodically extended image domain. For the solution domain bounded by a grounded conductor the image charges alternate between ± Q (denoted by red and blue). The entire image map is a periodic array because of the periodic boundary conditions. The electrostatic potential on the boundaries of the solution domain is zero.

Image Charge Assignment $Q_{image} = \lambda_{12}^{N} Q$

20	19	18	17	16	15	14	13	12	11	10	11	12	13	14	15	16	17	18	19	20
19	18	17	16	15	14	13	12	11	10	9	10	11	12	13	14	15	16	17	18	19
18	17	16	15	14	13	12	11	10	9	8	9	10	11	12	13	14	15	16	17	18
17	16	15	14	13	12	11	10	9	8	7	8	9	10	11	12	13	14	15	16	17
16	15	14	13	12	11	10	9	8	7	6	7	8	9	10	11	12	13	14	15	16
15	14	13	12	11	10	9	8	7	6	5	6	7	8	9	10	11	12	13	14	15
14	13	12	11	10	9	8	7	6	5	4	5	6	7	8	9	10	11	12	13	14
13	12	11	10	9	8	7	6	5	4	3	4	5	6	7	8	9	10	11	12	13
12	11	10	9	8	7	6	5	4	3	2	3	4	5	6	7	8	9	10	11	12
11	10	9	8	7	6	5	4	3	2	1	2	3	4	5	6	7	8	9	10	11
10	9	8	7	6	5	4	3	2	1	0	1	2	3	4	5	6	7	8	9	10
11	10	9	8	7	6	5	4	3	2	1	2	3	4	5	6	7	8	9	10	11
12	11	10	9	8	7	6	5	4	3	2	3	4	5	6	7	8	9	10	11	12
13	12	11	10	9	8	7	6	5	4	3	4	5	6	7	8	9	10	11	12	13
14	13	12	11	10	9	8	7	6	5	4	5	6	7	8	9	10	11	12	13	14
15	14	13	12	11	10	9	8	7	6	5	6	7	8	9	10	11	12	13	14	15
16	15	14	13	12	11	10	9	8	7	6	7	8	9	10	11	12	13	14	15	16
17	16	15	14	13	12	11	10	9	8	7	8	9	10	11	12	13	14	15	16	17
18	17	16	15	14	13	12	11	10	9	8	9	10	11	12	13	14	15	16	17	18
19	18	17	16	15	14	13	12	11	10	9	10	11	12	13	14	15	16	17	18	19
20	19	18	17	16	15	14	13	12	11	10	11	12	13	14	15	16	17	18	19	20

Figure 13. Image charge assignment for the image map of Figure 12. The central value N=0 corresponds to the source charge Q. The central square portion corresponds directly to the 100 locations shown in Figure 12. The 4 nearest neighbour image charges to the source charge Q have image charges $\lambda_{12}Q$ i.e *N*=1. The 4 next nearest neighbour image charges (N=2) have values $\lambda_{12}^{2}Q$.

Since the factor $\lambda_{12} = \dfrac{\varepsilon_1 - \varepsilon_2}{\varepsilon_1 + \varepsilon_2} \Rightarrow |\lambda_{12}| \leq 1$ the total potential in the solution domain converges.

These cases include a grounded conducting gate wrapping around the central dielectric core. The self-energy expressions are simple generalisations of the truncated series expansions over images.

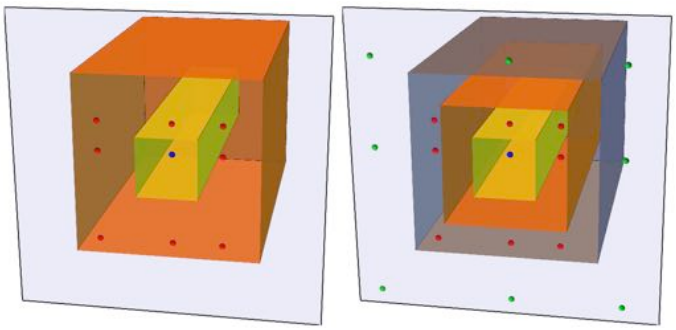

(a) (b)

Figure 14 (a): a point charge Q (blue) is located within an infinitely long finite square cross-section dielectric ε_1 (yellow) embedded in an infinite dielectric $0<\varepsilon_2<\varepsilon_1$ (orange). The nearest and next nearest image charges due to the 4 interfaces are shown in red in the image plane (light blue).
Figure 14 (b): a point charge Q (blue) is located within an infinitely long finite square cross-section dielectric ε_1 (yellow) embedded in an infinite dielectric ε_2 (orange) of finite thickness which in turn is embedded in a grounded conducting medium (gate). The nearest and next nearest image charges are shown in red in the image plane (light blue) arising from the first 4 interfaces; a further set of image charges (in green) that arise from the second set of interface at the gate boundary.

To illustrate, consider the following expression (30) for the self-energy in a two dielectric wrap-around geometry (Figure 14a) along the z-symmetry axis in a truncated expansion and without re-normalisation being applied.

$$\Sigma = \frac{Q^2}{16\pi\varepsilon_1}\frac{1}{b}\sum_{J=-N\max,\ J=K\neq 0}^{N\max}\ \sum_{K=-N\max}^{N\max}\frac{\lambda_{12}^{|J|+|K|}}{\sqrt{J^2+K^2}} \qquad (30)$$

Results for various materials configurations are shown in Figure 15.

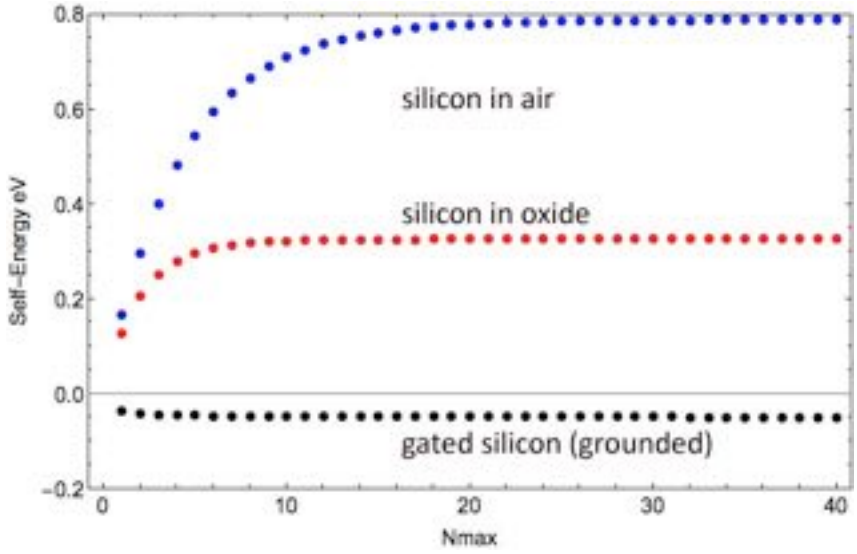

Figure 15 utilises equation (30) to compute the convergence of the self-energy for different materials configurations with boxed structure without re-normalisation and along the central axis ($x = y = 0$, arbitrary z). Here the silicon core is square with width = 2 nm.

4.2 Re-normalised model

The renormalisation procedure of section 3.4 permits the following simple expression for the re-normalised self-energy in boxed structures. Assuming that the value Σ_0 along the central axis is known accurately, the re-normalised result for a truncation index $N_{\max} \sim 2$ is:

$$\Sigma_R(x,y,z) = \Sigma_0 + \Sigma_1(x,y,z) - \Sigma_1(0,0,0) \tag{31}$$

$$\Sigma_1(x,y,z) = \frac{Q^2}{8\pi\varepsilon_{Si} b}\lambda_{12}\{\frac{b^2}{b^2-x^2} + \frac{b^2}{b^2-y^2} + (\lambda_{12}/2)\Lambda(x,y)\} \tag{32}$$

$$\Lambda = \frac{b}{\sqrt{(b-x)^2+(b-y)^2}} + \frac{b}{\sqrt{(b-x)^2+(b+y)^2}} + \frac{b}{\sqrt{(b+x)^2+(b-y)^2}} + \frac{b}{\sqrt{(b+x)^2+(b+y)^2}} \tag{33}$$

The expressions (31-33) give highly accurate results (better than 1%) across the full spatial domain where the nearest and next nearest neighbour images provide the spatial variation. The distant images contribute primarily to the central axis self-energy.

4.3 Gated dielectric wrapped around a square cross-section, long dielectric wire.

Figure 14b illustrates the generalisation to a *gated* boxed structure important in field-effect nano-transistors and compares the nearest image charges in the image plane for a core charge Q showing the additional images that derive from reflection at the upper interfaces. The inner interfaces are separated by the planes $x=b$, $x=-b$, $y=-b$, $y=b$ and by the set $x=a$, $x=-a$, $y=-a$, $y=a$ where $a=b+t > b$.

In analogy to section 3.1 the presence of the $I_{3\text{-}2}$ interface (gated-dielectric) leads to image charges arising from multiple internal reflections in the I_2 region in the ray construction of the images. Following the analysis of section 3 it is straightforward to utilise a simple re-normalisation of the lowest order images arising from internal reflection at the gate. The additional terms are similar in structure to expressions (20) and (23). Further to the simple example of section 3 there are also additional multiple reflections that derive from intermediate reflections at the inner boundaries. Despite the complexity, the multiple images contribute very little to the self-energy except along the central axis. This is a consequence of the large distances of the image charges involved. The simple re-normalisation scheme outlined in section 4.2 reduces the complexity of the self-energy to just a few simple analytical terms. Expressions (31-33) are then modified to order λ_{12} and for $|x| < b$, $|y| < b$ as:

$$\Sigma_1(x,y,z) = \frac{Q^2}{8\pi\varepsilon_{Si}b}\{\lambda_{12} - \frac{(1+\lambda_{12})b}{b+t}\}\{\frac{b^2}{b^2-x^2} + \frac{b^2}{b^2-y^2}\} \qquad (34)$$

Here t is the thickness of the dielectric I_2 separating the core I_1 from the gate. Letting $t \to 0$ in (34) recovers the simple grounded box result of sections 4.1 and 4.2. In the limit $t >> b$, we recover the self-energy for the un-gated dielectric box (section 4.1).

5. Application to wrap-round gate nanowire devices.

Realistic devices are finite heterostructures. An example is shown in exploded form in figure 16: a wrap-round gate silicon nanowire field effect transistor [15]. The source and drain regions ultimately contact a macroscopic system. The active region is the channel region under the gate. Here the silicon wire is a uniform homogeneous dielectric (although it is likely to be heavily doped in the source and drain regions). However, the dielectric environment of an electron in the silicon wire changes dramatically along the transport axis of the structure. At first sight there is scant hope of obtaining a simple image representation.

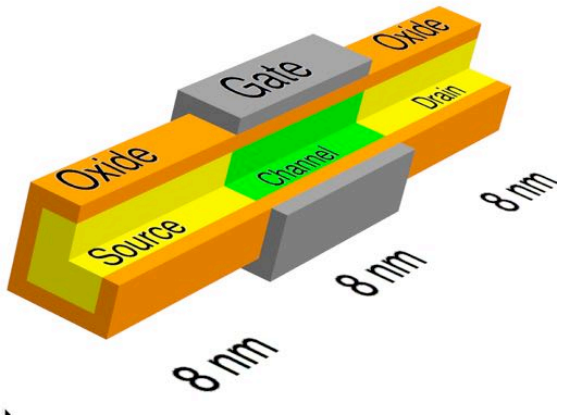

Figure 16. Schematics of a typical wrap round gate silicon nanowire field effect transistor.

5.1 Connecting the self-energies

Earlier sections have sketched how simple but accurate image charge models can be used to describe various infinite 3D nanowire dielectric structures. Thus it is straightforward to build a compact analytical model of long examples of each sub-component of a nanowire transistor, for example the self-energy variation along the central axis of a long source or drain region (e.g silicon in air or oxide), and for a long channel region (gated oxide surrounding silicon region). But it remains to join these disparate regions together to maintain the continuity of the self-energy and its longitudinal spatial derivative along the transport axis. The first procedure is to determine the self-energies for the long versions of the source, drain and gated channel that are independent of the transport direction z. The terms s*bulk*, *cbulk* and *dbulk* will refer to the self-energies derived from the long structures where the self-energies are independent of z. The origin of coordinates is taken to be in the centre of the channel at (0,0,0). Thus the source-gate edges are at $z=\pm L_g/2$ where L_g is the gate length.

A viable model for the self-energy throughout the full length of the central dielectric (silicon in our example) must satisfy physical continuity conditions on the self-energy and its gradient along the transport direction z (following from the continuity of the electrostatic potential and its gradient across a homogeneous dielectric region). To proceed we outline a heuristic model based on standard field-theoretic principles [16].

Consider a charge Q at (x_1,y_1,z_1) within a very long box (dielectric region E1) $-b < x_1 < b, -b < y_1 < b, -\infty < z_1 < \infty$ surrounded by a mismatched dielectric region E2 . In field theoretic terms we determine the self-energy in E1 by computing the total electrostatic potential $\phi(\mathbf{r},\mathbf{r}_1)$ in region E1. Here the general solution is a particular solution to Poisson's equation (the Coulomb potential) plus a general solution to Laplace's equation in E1. The Laplace equation is separable ($\phi(x,y,z) = \phi_X(x)\phi_Y(y)\phi_Z(z)$) in E1 and takes the form:

$$\frac{\mathrm{d}^2\phi_X}{\mathrm{d}x^2} = -k_x^2\phi_X;\ \frac{\mathrm{d}^2\phi_Y}{\mathrm{d}y^2} = -k_y^2\phi_Y;\frac{\mathrm{d}^2\phi_Z}{\mathrm{d}z^2} = -k_z^2\phi_Z \tag{35}$$

These equations are equivalent to Laplace's equation if the separation constants satisfy

$$k_x^2 + k_y^2 + k_z^2 = 0 \tag{36}$$

To satisfy (36) we choose:

$$k_z^2 = -k^2 = k_x^2 + k_y^2; \qquad \frac{\mathrm{d}^2\phi_Z}{\mathrm{d}z^2} = k^2\phi_Z \tag{37}$$

Solutions to (37) are of the form:

$$\phi_Z(z) \sim \exp[\pm kz],\ \ k = \sqrt{k_x^2 + k_y^2} \tag{38}$$

The transverse functions ϕ_X, ϕ_Y are complex exponentials or combinations of sines and cosines.

For a grounded box (region E2 =grounded conductor) the transverse functions must vanish at the interfaces leading to conditions

$$\begin{aligned} &k_x = k_n = n\pi / b \quad \text{(sin function)};\ (n+1/2)\pi / b \ \text{(cos function)} \\ &k_y = k_m = m\pi / b \quad \text{(sin function)};\ (m+1/2)\pi / b \ \text{(cos function)} \\ &k^2 = k_{mn}^2;\quad k_{mn} = \sqrt{k_m^2 + k_n^2}\ ;\ W = 2b. \end{aligned} \tag{39}$$

The lowest mode has

$$k_{00} = \frac{\pi\sqrt{2}}{2b} = \frac{\pi\sqrt{2}}{W} \tag{40}$$

It may then be shown that

$$\phi \sim \phi^T(x,y)\frac{\exp[-k_{00}\,|\,z - z_1\,|]}{2k_{00}} \tag{50}$$

which is valid for $|\,z - z_1\,| > 1/k_{00}$ and where z_1 is the location of Q.

Returning to the general case of a box E1 embedded in E2 , if $|\,\lambda_{12}\,| > 0.2$ we find from inspection of the image potentials obtained from the nearest image charges described in (32) that the lowest order k_x, k_y contributing to a Fourier decomposition are of the order of π/W which again leads to k_{00} as a good indicator for the z-dependence in (50). At the interfaces the image potential may be used to compute the induced charge distribution on the interface using Poisson's equation driven by the effective interface charge density $\rho(z)$. For a given image charge Q_I at $\boldsymbol{r}_I$ we obtain an interface charge density as a function of z, normalised to Q_I :

$$\rho(z) = (k/2)\exp[-k\,|\,z - z_1\,|]Q_I \tag{51}$$

This function is plotted in Figure 17(a), we choose the nearest image charge $Q_I = Q\lambda_{12}$ =0.8 (arbitrary units).

Suppose now the medium E_2 is replaced by a third dielectric E_3 in the region $|x|,|y| > b$ and $z>L_1$ creating an external dielectric corner at (see Figure 17(b). We make the *adiabatic approximation* that the charge density is *discontinuous* at $z=L_1=0.5$:

$$\rho(z) = (k/2)\exp[-k\,|\,z - z_1\,|]Q\{\lambda_{12} + (\lambda_{13} - \lambda_{12})\theta(z - L_1)\} \tag{52}$$

where we set $\lambda_{12}Q = 0.4$ (arbitrary units). Integrating over all z we find the effective image charge as the *continuous* function

$$Q_I(z_I) = Q\lambda_{12}\{1 - f_D(z_I, L_1)\} + Q\lambda_{13}f_D(z_I, L_1) \tag{53}$$

where the function f_D is

$$f_D(z, z_1) = (1/2)\exp[-k\,|\,z - z_1\,|] + (1 - \exp[-k\,|\,z - z_1\,|])\theta(z - z_1) \tag{54}$$

f_D and its first derivative are *continuous* at the interface $z=z_1$ as required from continuity of the image potential. Figure 18 plots the effective image charge $Q_I(z)$ as a function of source charge position z in a dielectric 1 enclosed by dielectrics 2 and dielectric 3 in a boxed structure with a dielectric mismatch between regions 2 and 3 at L=0.5.
The contribution to the total self-energy and its gradient with respect to z due to this image charge thus varies *continuously* with z as

$$\delta\Sigma(x,y,z) = \Sigma_{12}(x,y)\{1 - f_D(z,L_1)\} + \Sigma_{13}(x,y) f_D(z,L_1) \qquad (55)$$

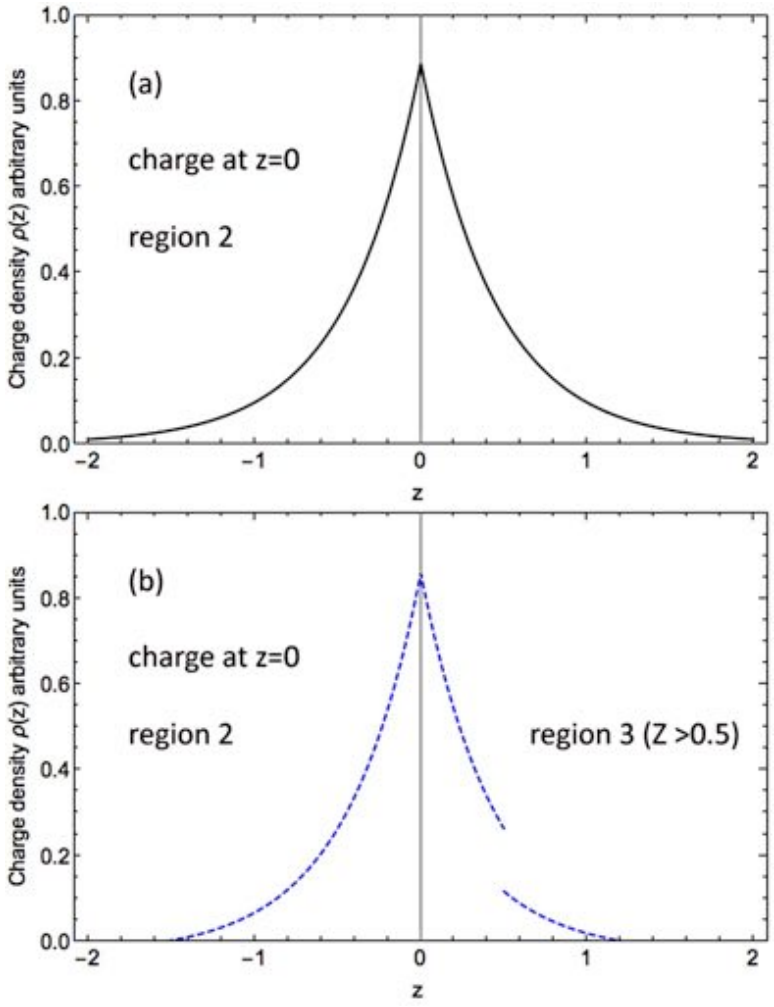

Figure 17. (a) Model induced charge density at an interface between a dielectric 1 and a dielectric 2 in a boxed structure. Source charge at z=0 in region 1. (b) Model induced charge density at an interface between a dielectric 1 and a dielectric 2 ($z<L$ =0.5) and a dielectric 3 (z >0.5) in a boxed structure. Note the discontinuity at $z=L$. Decay constant $k = \sqrt{2}\pi / W$ for W=2.

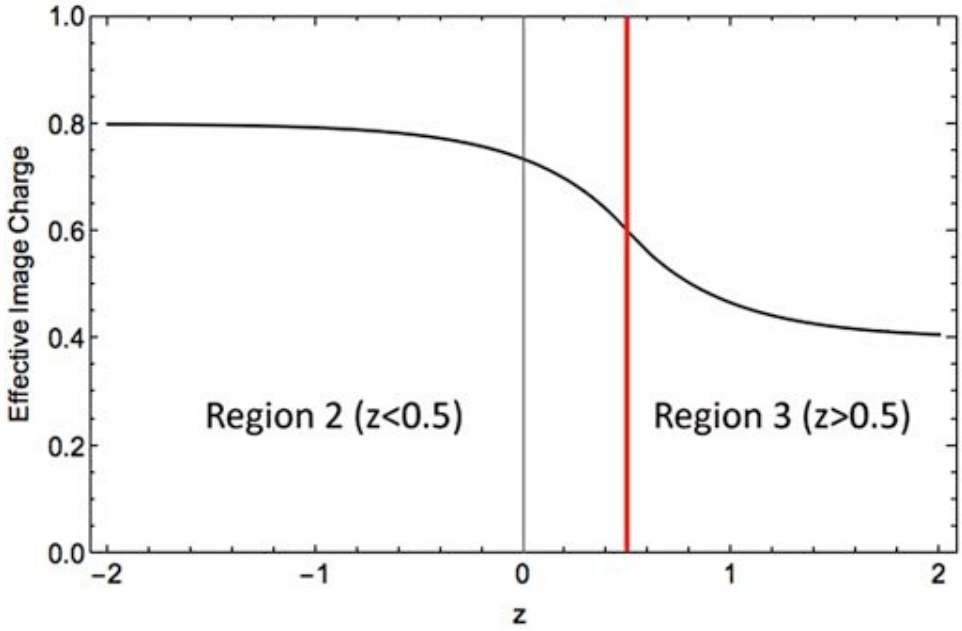

Figure 18. Effective Image charge $Q_I(z)$ as a function of source charge position z in a dielectric 1 enclosed by dielectrics 2 and dielectric 3 in a boxed structure with a dielectric mismatch between regions 2 and 3 at L=0.5. The effective image charge in a long boxed structure involving dielectrics 1 and 2 only is set arbitrarily at $Q\lambda_{12}$=0.8; for dielectrics 1 and 3 alone $Q\lambda_{13}$=0.4. Decay constant $k = \sqrt{2}\pi / W$ for W=2.The transition region is approximately of width 2/k.

Extending the same argument to a further dielectric mismatch at L_2 where region E_4 onsets leads to:

$$\delta\Sigma(x,y,z) = \Sigma_{12}(x,y)\{1 - f_D(z,L_1)\} + \Sigma_{13}(x,y)\{f_D(z,L_1) - f_D(z,L_2)\} + \Sigma_{14}(x,y) f_D(z,L_2) \tag{56}$$

Finally summing over all the image charges we obtain the total self-energy as the approximation:

$$\Sigma(x,y,z) =$$
$$\Sigma_{sbulk}(x,y)\{1 - f_D(z,-L_g)\} + \Sigma_{cbulk}(x,y)\{f_D(z,-L_g) - f_D(z,L_g)\} + \Sigma_{dbulk}(x,y) f_D(z,L_g) \tag{57}$$

This approximation is and its first derivatives are continuous in z within the central dielectric box and reduce to the long sample expressions in the limits
$(|z| >> L_g \ (L_g \ \text{finite}); |z| << L_g (L_g \to \infty)$.

The function f_D is an example of a representation of the distribution $\theta(z - z_1)$. The logistic function f_L is similar in form:

$$f_L(z,z_1) = \frac{1}{1 + \exp[-k(z - z_1)]} \qquad (k > 0) \tag{58}$$

Figure 19(a) shows the field theoretic model for the self-energy at *(x=y=0)* along the central transport direction *z* of a hypothetical nanowire field-effect transistor for which $\Sigma_{sbulk} = \Sigma_{dbulk} = 0.15eV, \Sigma_{cbulk} = 0.05eV, Lg = 4nm, W = 2nm, k = 2\sqrt{\pi / W}$. For comparison we show the result of replacing f_D by an empirical logistic function f_L with the same parameters.

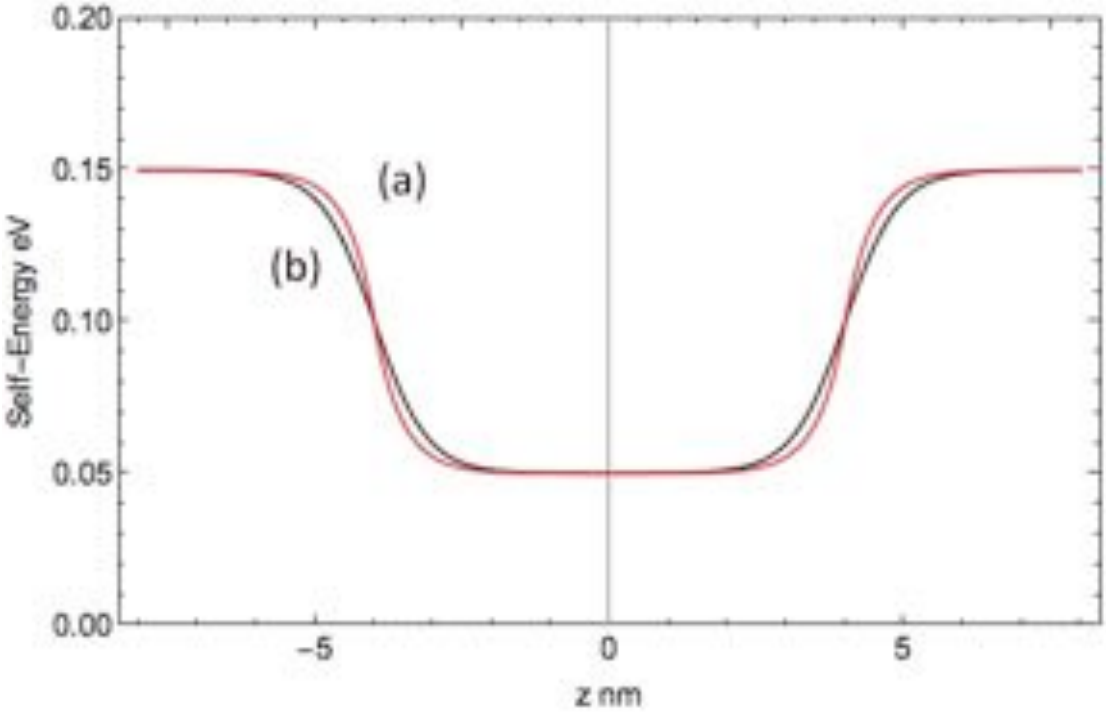

Figure 19 (a) In red: field theoretic model for a continuous self-energy along the central transport axis of a hypothetical wrap round gate transistor. (b) In black: Empirical logistic model with identical parameters to (a)

The results of Figure 19 are very similar to numerical computations for the self-energy within a nanowire transistor [2, 9].

A complete image-based model for the nanowire field effect transistor is obtained by inserting expressions (31-33) appropriate to the source, gated channel and drain into expression (57). Figure 20 shows a representation of the self-energy for a typical set of device parameters.

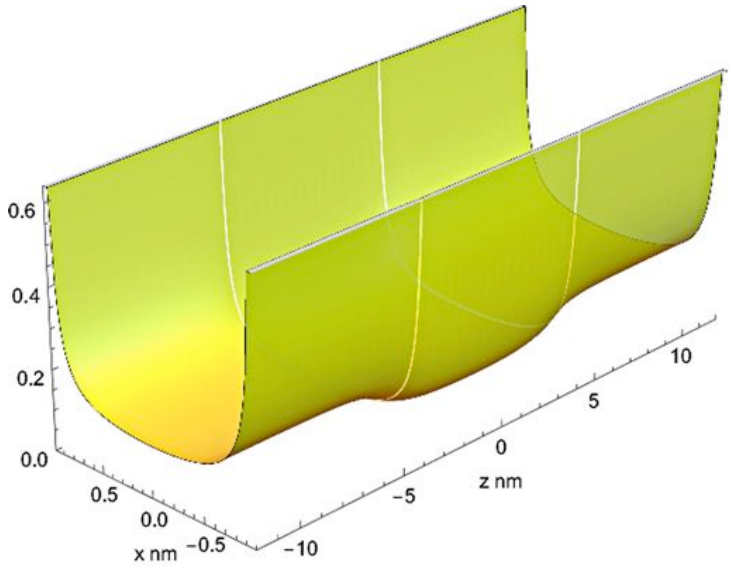

Figure 20. Model electrostatic self-energy of a silicon based nanowire field effect transistor $\Sigma(x,\ y=0,\ z)$ showing a section along the transport axis in *x-z* plane. Gated oxide thickness t = 1 nm; silicon thickness $W=2b$ = 2 nm; z-axis length = 24 nm; Lg=4 nm. Position of gate boundaries illustrated by white lines. $k=\sqrt{2}\pi / W$

6. Extensions

The image methodology may be extended to cylindrical geometries [17, 18] with important string charge extensions. Figures 21, 22 compare the self-energy for a square cross section silicon based wrap round gate field effect transistor with that for a comparable cylindrical device of the same cross-sectional area. The results show very similar dependence on z, and in the central region $r=\sqrt{x^2+y^2} < W/4$. Figure 21 shows self-energy contours in the x-y plane at z=0 and Figure 22 shows the self energy contours in the x-z plane at y=0.

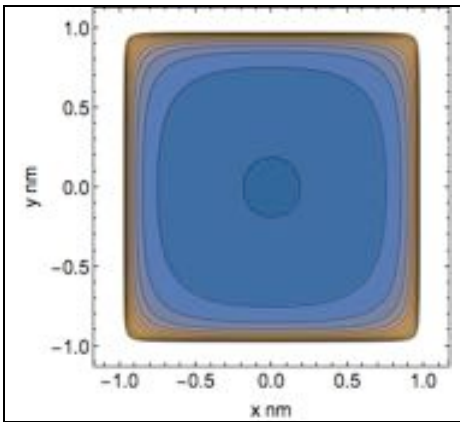

Figure 20(a) Energy contours of the electrostatic self-energy in cross section of rectangular wrap-round gate device for *z*=0 (device centre).

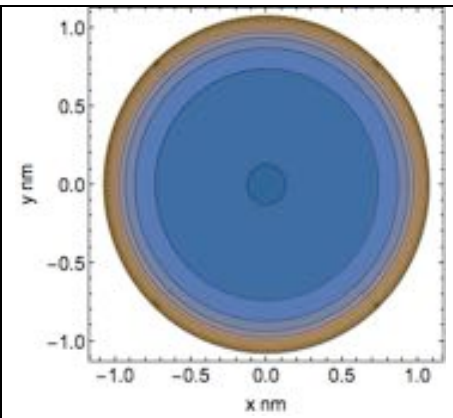

Figure 20(b) Energy contours of the electrostatic self-energy in cross section of a cylindrical wrap-round gate device for *z*=0 (device centre).

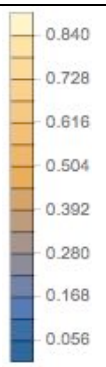

Energy scale in eV

Silicon channel thickness (W) = 2 nm, Oxide thickness = 1 nm. Channel cross sectional area = 4 nm^2	Silicon core radius = 1.1284 nm, Oxide thickness = 1 nm. Channel cross sectional area = 4 nm^2	

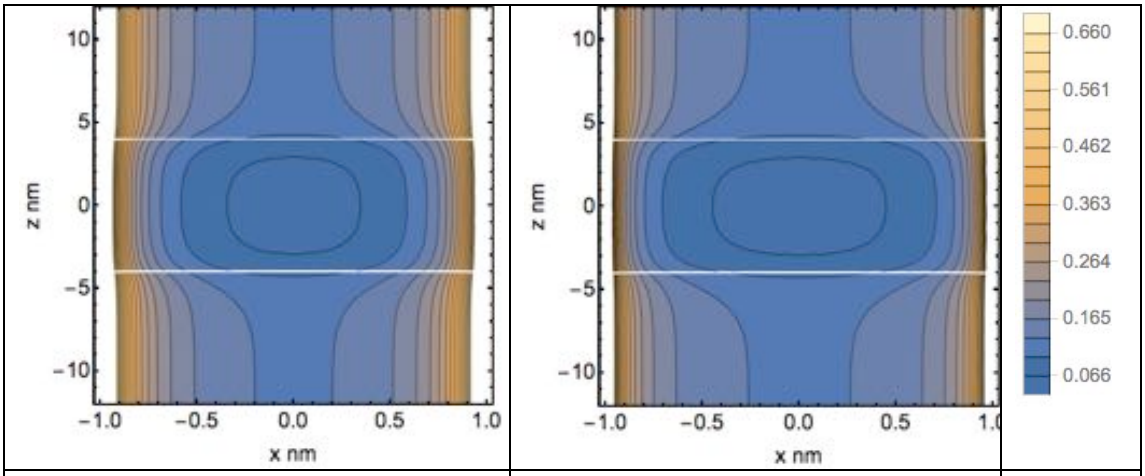

Figure 21(a) Contours of self-energy in the *x-z* plane (*y*=0) for the rectangular nanowire structure. White lines demarcate gated channel region.	Figure 21(b) Contours of self-energy in the *x-z* plane (*y*=0) for the cylindrical nanowire structure. White lines demarcate gated channel region.	Energy scale eV

7. Discussion and Conclusions

We have demonstrated that image charge modelling provides compact, accurate, analytic computation of the electrostatic self-energy in square or rectangular cross sectional 3D geometries suitable for a range of nanowire heterostructures. We have shown that the image method works well for the electrostatic self-energy due to its dependence on the diagonal (or local) limit of the classical electrostatic Green functions. In contrast, computation of the electrostatic potential at large separations from the source charge renders the image method conditionally convergent, cumbersome and numerically intensive. It has been further shown that nanowire geometries the self-energy dependence on the transverse distance from central longitudinal transport axis is generally determined by contributions from the nearest and next nearest images. The central axis self-energy depends on a large number of images. The self-energy has been shown to be computable to very high accuracy using a renormalisation technique that reduces the complexity of the computations. A new technique for matching different heterostructure geometries has been demonstrated that permits the modeling of complicated device structures.

It was pointed out that simple classical interfaces that are not atomically resolved give rise to divergences in the self-energy. These divergences have no impact on most device modeling situations as they correspond to regions where carriers are not present. In the case of tunneling across interfaces, where the divergence is important, it is straightforward to replace the classical interface by an atomically resolved method without loss of generality of the image method. This refinement has already been noted in full-scale numerical computations [7 Appendix B]. Older methods [24, 25] of removing the divergence introduce discontinuities and distortion on the farther side of an interface.

Challenges for future work include extending the image charge model formalism to defects or ion contamination in nanostructures interfaces and to atomistic randomly sited impurities. The key factor here is whether or not this may be achieved by a simple change to the dielectric constant within the perturbed region. If the perturbation region is sufficiently polarizable that

may be possible. The effect of electrostatic self-energy on tunneling through interfaces has a long history reaching back over 30 years [26]. However, the existence of simple image charge methodology rather than using a full numerical approach via Poisson's equation is not yet clear. Part of the problem is that for curved interfaces the image charges may form complex line charges [Barker, unpublished].

In device modelling, the influence of the self-energy on self-consistent transport as a function of source, drain and gate voltages has been studied in reference [2, 9] and by us (using Keldysh Green functions, unpublished). The effects are manifest via the local self-consistent gate potential determined from Poisson's equation. The main effect is a distortion and lowering of the barrier potential.

Finally, it is observed that our methodology is applicable to a diverse range of heterostructures other than semiconductor nanowires. Examples include: quantum dot structures, carbon nanotubes and ion channels. There are also possibilities for investigation of image methods applied to the self-energy in nested stadiums for which chaotic ray paths are of interest.

Appendix

Here is sketched a derivation of an integral form for the exact solutions given by the infinite series (20) and (22) for the case $\lambda_{23} = -1$ (region 3 is a grounded conducting slab). Without loss of generality we locate the source charge Q in region 1 at y=0. The interface with region 2 is at $y=b$. The interface with region 3 is at $y=b+t$ (t=thickness of region 2).

Solving Poisson's equation in region 1 and Laplace's equation in region 2 leads to the general solutions in regions 1 and 2 in the form:

$$\varphi_1 = \frac{Q}{4\pi\varepsilon_1}\int_0^\infty J_0(k\rho)\{e^{-k|y|} + Ae^{ky}\}dk \qquad \text{(A1)}$$

$$\varphi_2 = \frac{Q}{4\pi\varepsilon_1}\int_0^\infty J_0(k\rho)\{Ce^{ky} + De^{-ky}\} \qquad \text{(A2)}$$

Here we have already applied the boundary condition $\varphi_1(y \to -\infty) = 0$. The boundary condition at the second interface requires the potential to be zero at $y=b+t$. Hence the coefficient D must satisfy

$$D\exp[-k(b+t)] = -C\exp[k(b+t)] \qquad \text{(A3)}$$

Thus

$$\varphi_2 = \frac{Q}{4\pi\varepsilon_1}\int_0^\infty J_0(k\rho)\{-2C\sinh[k(b+t-y)]e^{k(b+t)}\} \qquad \text{(A4)}$$

The coefficients A and C are determined by matching the functions φ, $\varepsilon\frac{\partial\varphi}{\partial y}$ at $y=b$.

For the self-energy we only require coefficient A which is

$$A(k) = \frac{\lambda_{12} - e^{-2kt}}{1 - \lambda_{12} e^{-2kt}} \qquad \text{(A5)}$$

where λ_{12} is defined by (15). The self-energy follows (Q/2) multiplied by the term in C at the location y=0 of the source charge:

$$\Sigma(y=0) = \frac{Q^2}{8\pi\varepsilon_1} \int_0^\infty J_0(k\rho) \{ \frac{\lambda_{12} - e^{-2kt}}{1 - \lambda_{12} e^{-2kt}} e^{-2kb} \} dk \quad (\text{limit } \rho \to 0) \qquad \text{(A6)}$$

Expression (A6) is an integral solution that may be computed numerically. The inverse denominator of (A6) may also be expanded as a power series in $\lambda_{12} \exp[-2kt]$ to obtain an infinite sum of exponentials that may be put in the form of Coulomb functions using (10).

$$\Sigma(y=0) = \frac{Q^2}{8\pi\varepsilon_1} \int_0^\infty J_0(k\rho) \{ (\lambda_{12} - e^{-2kt}) e^{-2kb} \sum_{N=0}^{\infty} \lambda_{12}^N e^{-2Nkt} \} dk \quad (\text{limit } \rho \to 0) \quad \text{(A7)}$$

Using representation (10) we express each term as a Coulomb term derived from individual image charges:

$$\Sigma(y=0) = \frac{Q^2}{8\pi\varepsilon_1} \{ \frac{\lambda_{12}}{2b} + \sum_{N=1}^{\infty} \frac{\lambda_{12}^{N+1}}{2(b+Nt)} - \sum_{N=0}^{\infty} \frac{\lambda_{12}^N}{2(b+(N+1)t)} \} \qquad \text{(A8)}$$

The first few terms are:

$$\Sigma(y=0) = \frac{Q^2}{16\pi\varepsilon_1} \{ \frac{\lambda_{12}}{b} - \frac{(1-\lambda_{12}^2)}{b+t} + \ldots\ldots \} \qquad \text{(A9)}$$

The first term involves the image of Q in the interface at y=b. The second term involves the contribution of the image in the second interface at y=b+t. The remaining terms involve multiple reflections.

Using the definition of percentage error:

$$E = 100 \frac{|\Sigma_{exact} - \Sigma_{approx}|}{\Sigma_{exact}}$$

we use a high precision evaluation of (A6) and whatever approximation is obtained for the sum over image terms.

References

[1] C. Delerue and M. Lannoo, *Nanostructures Theory and Modelling*, Springer (2004).

[2] C. Li, M. Bescond and M. Lannoo, Phys.Rev. B **80** 195318 (2009).

[3] A. Martinez, N. Seone, A. R. Brown, J. R. Barker and A. Asenov, IEEE Transactions on Nanotechnology, **8** 603 (2009).

[4] A. Martinez, N. Seone, A. R. Brown, J. R. Barker and A. Asenov, IEEE Transactions on Electron Devices, **57** 1626 (2010).

[5] A. Martinez, N. Seoane, M. Aldegunde, A. R. Brown, J. R. Barker And A. Asenov
IEEE Transactions on Electron Devices, **58** 2209 (2011).

[6] A. Martinez, A. Price, R. Valin, M. Aldegunde and J. R. Barker
Journal of Computational Electronics, **15** 1130 (2016).

[7] Y. M. Niquet, A. Lherbier, N. H. Quang, M. V. Fernández-Serra, X. Blase, and C. Delerue, Phys.Rev. B **73** 165319 (2006).

[8] C. Li, M. Bescond and M. Lannoo, Appl. Phys. Lett. **97** 252109 (2010).

[9] M. Bescond, *Semiconductor Nanowires*, ed. J. Arbiol and Q. Xiong, Elsevier, Chapter 6: *Quantum Transport in Semiconductor Nanowires* (2015).

[10] L. Hedin and S. Lundqvist, Solid State Phys. **23** 1 (1970).

[11] L. Hedin, B. L. Lundqvist and S. Lundquist, Solid State Communications, **9**, 537 (1971).

[12] W. Cai, *Computational Methods for Electromagnetic Phenomena*, Cambridge University Press, (2013).

[13] J. Pumplin, American Journal of Physics **37** 737 (1969).

[14] I. S. Gradshteyn and I. M. Ryzhik, *Table of Integrals, Series and Products*, ed. A. Jeffrey, Academic Press, Inc, 9.550, 1075 (1980).

[15] M. Aldegunde, A. Martinez and J. R. Barker, Journal of Applied Physics, **113** 014501 (2013)

[16] J. D. Jackson, *Classical Electrodynamics*, John Wiley and Sons, Inc, (1999).

[17] A. Martinez, J.R.Barker and M. Aldegunde
Int. *Workshop on Computational Electronics* 16, (ed N. Mori and S. Selberherr, 2013, Society for Micro-and Nanoelectronics, Technische Univeritat Wien:ISBN 978-3-901578-26-7) 50 (2013)

[18] J.R. Barker and A. Martinez, unpublished.

[19] D. Newns, J.Chem.Phys. **50** 4572 (1969)

[20] L.W. Lang, A. Zunger, Phys.Rev.Letters, **73** 1039 (1994)

[21] R. Tsu, D. Babic, Applied Phys. Letters, **64** 1806 (1994)

[22] M. Lannoo, C.Delerue,G.Allan; Phys.Rev.Letters **74** 3415 (1995)

[23] C.Delerue, M. Lannoo, G.Allan; Phys.Rev.B **68** 115411 (2003)

[24] M. Kumagai and T. Takagahara Phys Rev B **40** 12359 (1989)).

[25] Y. M. Niquet, C. Delerue, G. Allan, M. Lannoo, Phys. Rev. B **65** 165334 (2002)

[26] M.C. Payne and J.C. Inkson, Surface Science, **159** 485 (1985).